LES of the flow around a circular cylinder of finite height

Jochen Fröhlich

Institut für Technische Chemie und Polymerchemie, Universität Karlsruhe

Kaiserstrasse 12, 76128 Karlsruhe, Germany

froehlich@ict.uni-karlsruhe.de

Wolfgang Rodi

Institut für Hydromechanik, Universität Karlsruhe

Kaiserstrasse 12, 76128 Karlsruhe, Germany,

rodi@uka.de

Abstract

The paper presents large eddy simulations of the flow around a surface–mounted circular cylinder of height 2.5 times the diameter at a Reynolds number of $Re = 43000$. In the first part, the different modelling parameters are discussed with respect to their influence on the computed results. One of the findings is that, on the relatively coarse grid employed, the dynamic model is deficient and yields a too short recirculation region. The results obtained with the Smagorinsky model are in fairly good agreement with measurements. In the second part of the paper a detailed analysis of the results in physical terms is provided and related to findings in the literature. In particular, the existence of tip vortices and an arch vortex in the average flow downstream of the free end is demonstrated.

1   Introduction

The flow around bluff bodies such as wall-mounted cubes, cylinders, tube bundles, etc. has been attracting considerable interest due to its industrial relevance. Long bodies like cylinders of high aspect ratio typically lead to pronounced regular vortex shedding with the potential of creating resonances which in turn may provoke undesired flow features or even the failure of structures (Naudascher and Rockwell, 1994).

End effects alter the vortex shedding substantially and can mainly be grouped into those at free ends and those at a junction with a larger body or a wall. Both are encountered in case of a wall–mounted cylinder of finite height as sketched in Figure 1. Therefore, this flow is a prototype configuration which allows to study both effects and also the interaction between them. When reducing successively the height–to–diameter ratio H/D, the regular alternating vortex shedding being typical for a long cylindrical structure is, in an intermittent way, more and more replaced by symmetrically shed vortices in the range $H/D \approx 6$ to $H/D \approx 2$ (Kawamura *et al.*, 1984; Kappler, 2002). Vortex shedding is mostly suppressed for values around and below $H/D \approx 2$ (Okamoto and Yagita, 1973; Kappler, 2002). Compared to the case of an infinite cylinder, the number of influence parameters is substantially larger for cylinders of finite height. In addition to the Reynolds number Re and the free–stream turbulence level, the height–to–diameter ratio H/D and the thickness of the approaching boundary layer δ/H influence the flow as addressed by Kawamura *et al.* (1984) and subsequent publications. Due to the finite length of the body the average flow is, in contrast to the long cylinder, highly three–dimensional.

The interaction of different mechanisms of instability (like von Karman, Kelvin–Helmholtz, etc.) is a typical feature of bluff body flows. Here, the situation is further complicated by the end effects so that the detailed analysis of this flow is a substantial challenge. The aim of the present study is to perform large eddy simulations (LES) for this flow and to analyze its structure, and in particular the role and interaction of the various mechanisms.

2 Configuration investigated

The flow around a circular cylinder of finite height studied here corresponds to an experiment performed by Kappler (2002) in a water tunnel. The Reynolds number was $Re = 43000$, based on the cylinder diameter and the free–stream velocity u_∞. For a long cylinder in uniform flow this value falls into in the sub–critical, more precisely into the "upper Transition in Shear Layer" regime $Re = 2 \cdot 10^4, \ldots, 2 \cdot 10^5$ (Zdravkovich, 1997). This regime exhibits only small changes with Reynolds number and is characterized by a laminar boundary layer along the cylinder wall, laminar separation, and transition to turbulence in the shear layer shortly after separation through a Kelvin–Helmholtz instability and further spanwise instabilities. This scenario requires low turbulence approach–flow. It is relevant for the present case, since in the experiment the turbulence level was $Tu = 2\%$, and indeed was observed in both, experiment and simulation. Note that the Reynolds number is fairly high for an LES: the boundary layer along the cylinder surface is very thin but needs to be resolved.

Different ratios H/D were investigated in the experiment. Here, we select the case $H/D = 2.5$ so that according to the above discussion only a small amount of regular vortex shedding is to be expected. The boundary layer thickness of the approaching flow was $\delta/H = 0.1$ which is small and different from applications in building aerodynamics. The width of the tunnel was $7D$ and the height $5D$ introducing a blockage of $Bl = 7.3\%$.

The available experimental data result from two–component LDA measurements in different horizontal and vertical planes. The measured quantities are the streamwise velocity component together with a second component, depending on the orientation of the laser beam, and in each case the corresponding fluctuations.

3 Numerical method and LES modelling

The simulations have been performed with the code LESOCC2 which is a successor of the code LESOCC (Breuer and Rodi, 1996) and solves the incompressible Navier–Stokes equations on curvilinear block–structured grids. A collocated Finite–Volume discretization with second order central schemes for convection and diffusion terms is employed. Temporal discretization is performed with a three–stage Runge–Kutta scheme solving the pressure–correction equation in the last stage only.

Table 1 provides an overview over the simulations performed. Two subgrid–scale models have been employed in these computations. One is the Smagorinsky model (SM) based on an eddy viscosity $\nu_t = l^2 |S|$ where $S = (\partial_{x_i} u_j + \partial_{x_j} u_i)/2$ and $|S| = \sqrt{2 S_{ij} S_{ij}}$ (overbars designating resolved quantities are dropped throughout the present text). This model is employed with van Driest damping so that the length scale l reads

$$l = C_s \Delta (1 - \exp(-y^+/25)^3)^{1/2} \tag{1}$$

with $\Delta = (Vol)^{1/3}$ and Vol the volume of a computational cell. A standard value for the constant is $C_s = 0.1$ (Moin and Kim, 1982) which also is in the range of the optimal value observed by Meyers *et al.* (2003). The second subgrid–scale model is the dynamic Smagorinsky model (DSM) of Germano *et al.* (1991), here employed with least squares averaging and three–dimensional test filtering. The test–filtered data were obtained by integration over volumes twice as large as the grid cells by means of the trapezoidal rule. This operation was performed without accounting for stretching and curvature as these are of secondary importance in typical LES grids. It results in weighting the central cell with 1/8 and the neighbouring cells with 1/16, 1/32, 1/64, depending on their respective location and appropriately modified near the walls. Since the flow does not feature any homogeneous direction the eddy viscosity was regularized according to $\nu_t^{n+1} = \varepsilon\nu_t^* + (1-\varepsilon)\nu_t^n$ with ν_t^* being the preliminary value determined from the standard dynamic procedure and $\varepsilon = 0.001$ (Breuer and Rodi, 1996) and imposing $0 \le \nu_t \le 100\nu$ where ν is the molecular viscosity.

The width and the height of the computational domain were selected to be the same as in the experiment, hence introducing the same blockage. With the base of the cylinder located at the origin of the coordinate system and x, y, z representing the streamwise, wall–normal and lateral direction, respectively, this yields $y/D = 0, \ldots, 5$ and $z/D = -3.5, \ldots, 3.5$ (see Figure 2). The outflow boundary is located at $x/D = 12.5$ where a convective boundary condition was imposed. The upstream boundary condition is located at $x/D = -7.5$ where a constant velocity $u = u_\infty$ was imposed (no fluctuations). Such a condition has been used successfully already for the simulation of subcritical flows around long cylinders (Fröhlich *et al.*, 1998) and is justified here for the case of negligible turbulence level at the entry and a very thin bottom–wall boundary layer. The boundary condition on the cylinder surface was a no–slip condition in all computations. The conditions at the top wall and at the sidewalls were free–slip conditions.

The first two computations, G1SS and G2SS, employed a frictionless ground plate which is equivalent to imposing a symmetry plane. Consequently, no boundary layer develops along the bottom wall, but the flow around the free end can be investigated (Fröhlich *et al.*, 2002). Two grids were used, a coarse grid (G1) with 1 Mio. points and a finer grid (G2) with 6.4 Mio. points partitioned into 24 blocks. The latter is displayed in Figure 2. The same grid was then used imposing a solid ground plate with friction using the Werner and Wengle (1993) wall function. Typical average values of y^+ are around $40 \ldots 80$, remote from separation and reattachment zones. With this condition a small boundary layer develops along the bottom wall. It has been compared to measurements in the empty tunnel and found to exhibit similar profiles of mean and fluctuating streamwise velocity. In another computation the impact of the subgrid–scale model was investigated by employing the dynamic model. The time step in all simulations was adjusted instantaneously according to the stability criterion of the time scheme which yielded values around $10^{-3}D/u_\infty$.

4 Results

The impact of the different numerical and modelling parameters on the results will be discussed first by means of averaged quantities. Figure 3 compares profiles of streamwise mean velocity and related fluctuations for the different runs to the experimental data. Figures 4 and 5 show average streamlines and fluctuations for G2SS and G2WS in comparison with those from the experiment. All quantities are given in units of D for lengths, u_∞ for velocities, and D/u_∞ for time.

Table 1 reports the mean drag coefficient $C_D = f_x/0.5\rho u_\infty^2 LD$ which can serve as a first criterion for assessment. The temporal evolution of lift and drag force f_z and f_x, respectively, is depicted in Figure 9 below for run G2WS. These forces have been computed by integrating wall pressure and friction over the cylinder surface at each time step. The latter contribution is substantially smaller than the former, as expected. Experimental values for C_D have been obtained almost exclusively by integration of the pressure over the surface, neglecting the viscous contribution as in Farivar (1981); Kawamura *et al.* (1984); Okamoto and Sunabashiri (1992) and others. It is generally observed that C_D decreases when reducing H/D due to the intrusion of the flow over the top into the wake. On the other hand, the drag increases with reduced boundary layer thickness δ/H and also depends on the free stream turbulence level and the blockage Bl, similar to the case of the long cylinder. Hence, for the particular set–up calculated it is hard to find exactly matching conditions in the literature. In the companion experiment of Kappler (2002), surface pressures or forces could not be measured. Experimental values from situations similar to the present one are $C_D = 0.78$ ($H/D = 2, \delta/H = 0.1, Bl = 0.88\%$, (Kawamura *et al.*, 1984)) and $C_D = 0.73$ ($H/D = 2, \delta/H = 0.1, Bl = 1.3\%$, (Okamoto and Sunabashiri, 1992)) in the same Reynolds number regime. The fairly large influence of the blockage ratio can be appreciated by reference to the value $C_D = 1.22$ measured by Baban and So (1991) ($H/D = 2, \delta/H = 0.1, Bl = 11.2\%$). In light of these data the present value of $C_D = 0.88$ obtained by simulation G2WS for a blockage ratio of $Bl = 7.3\%$ can be considered to be in good agreement with the literature.

4.1 Influence of the grid

A comparison of runs G1SS and G2SS in Table 1 shows the drastic effect of insufficient resolution. Streamline plots (not displayed here) reveal that the shear layers separating from the cylinder are shifted towards the symmetry plane due to delayed separation, the wake narrows and as a consequence the drag is substantially reduced. The Smagorinsky model, when employed with the finer grid G2, yields a reasonable match with the experiment as shown by the results given in Figures 3 to 5. This is improved further when friction at the bottom wall is accounted for.

4.2 Influence of the subgrid–scale model

The Reynolds number is high and the grid G2 in the upstream part and along the cylinder wall is still relatively coarse for a wall–resolving LES. When switching to the dynamic model, the test filter operation projects the velocity onto an even coarser grid. The underresolution is most critical for the (laminar) shear layers separating from the cylinder along the sides as experienced in earlier work on long cylinders (Fröhlich *et al.*, 1998, 2001). With the DSM, a larger eddy viscosity is produced compared with the SM and the present value of C_s, yielding a shift of the shear layers towards the symmetry plane and hence a reduction of the drag (see Table 1), similar to the effect of using a coarse grid, but not as strong. Further, in the wake the DSM generated larger values of ν_t than the SM, e.g. by about a factor of 4 in the locations considered in Figure 3.

4.3 Influence of the bottom wall boundary condition

We now address the influence of the bottom wall boundary condition which can be assessed by comparison of runs G2SS and G2WS. The wall boundary layer is thin, with $\delta/H \approx 0.1$

so that the effect of accounting for its development is small. In particular, the flow upstream of the cylinder is little affected as evidenced by the low position of the saddle point on the stagnation line and the thin horseshoe vortex shown in Figures 11 and 12 below. However, in the rear of the cylinder the bottom boundary condition can have some influence on the evolution of the shed vortices. In order to investigate this, cuts normal to the streamwise axis are displayed in Figure 6 for a calculation with (right) and without (left) bottom wall. They have been generated at $x/D = 1$, $x/D = 2$ and $x/D = 3.5$ and these locations are indicated in Figure 5. The upper graphs in Figure 6 at $x/D = 1$ show that the wake narrows somewhat near the lower boundary if this is a solid wall. Also, accounting for the bottom boundary layer appears to improve somewhat the streamline pattern in the recirculation zone behind the cylinder (Figure 5). At $x/D = 2$, the difference between the calculations might seem very large, due to the appearance of two foci in the left picture, but it should be noted that the plane $x/D = 2$ is close to the reattachment point on the bottom as revealed by Figure 5. This introduces a marked sensitivity of the streamlines with respect to the exact position considered which is responsible for this visually different impression. At $x/D = 3.5$, the trailing vortices are almost circular in the case with slip while being more elliptic in the case with a solid wall. Further discussion of this figure is provided in Section 4.5 below.

4.4   Instantaneous flow

An impression of the instantaneous flow is given by Figure 7 from G2WS displaying an iso–surface of the normalized instantaneous deviation of the pressure from the average $\tilde{p}' = (p - \langle p \rangle)/(\rho u_\infty^2)$. This visualization of the flow structure was complemented by further views and animations upon which the following comments are based. They show the separation at the sharp front corner of the cylinder top to be fairly regular, exhibiting lateral vortex rollers which inter–wind and merge upon travelling downstream along the roof. Around the rear of the top end the separation process is highly complex and very irregular due to the curved trailing edge and the separation at the sidewalls so that organized motion can hardly be detected. Near the top, the separation along the cylinder shaft is similarly influenced by the flow over the free end but becomes more regular further down towards the bottom wall. There, the separation takes place in a more coherent way and larger vortices with their axis parallel to the cylinder axis are formed. In the experiment no regular vortex shedding was detected near the top end but regular alternating shedding near the bottom surface for all height–to–diameter ratios (Kappler, 2002). For $H/D = 2.5$, symmetrical vortex shedding did occur occasionally near the bottom in rare events. Figure 8 presents a tracer photograph near the bottom plate from the experiment and a plot from G2WS showing the instantaneous $u-$velocity at an instant with alternating vortex shedding. The qualitative agreement between both is good.

Further downstream in the wake the shed vortices increase in size and become smoother. Highly distorted von Karman vortices are visible in Figure 7. They are bent inwards and backwards due to the downward motion behind the cylinder visible in the streamline pictures of Figure 5. Plots such plots viewed from the side as well as plots of the instantaneous pressure in planes $y = const$ (not shown here) reveal that alternating vortex shedding persists up to $y/D \approx 1.5$. Above this height, perturbations exhibit only small scales and are restricted to the close vicinity of the cylinder due to the strong downward motion behind the cylinder. Comparison with the sketches in Figure 1 shows that for the present aspect ratio regular alternating vortex shedding is not observed over a substantial portion of the shaft, with vortex axes parallel to the cylinder. Alternating vortices, however, are still present behind the lower

part of the cylinder as also observed in the experiments. The concept visualized in Figure 1 therefore should possibly be completed with this feature.

The irregular separation and shedding processes produce relatively irregular forces on the cylinder. This is illustrated in Figure 9 by showing the temporal evolution of the instantaneous lift and drag forces for G2WS (corresponding pictures for the other runs look similar, but with different average values of the coefficients). A dominant frequency f with a Strouhal number of about $St = fD/u_\infty = 0.16$ can be discerned from the lift coefficient while the drag exhibits twice this frequency as usually observed for this type of flow (Jordan, 2002). The lift coefficient exhibits an irregularly changing amplitude and can have an average different from zero over a certain number of shedding periods. This is a demanding situation and requires long averaging times, making the computations very expensive. An irregularity in the forces on the cylinder is usually also observed for a long cylinder even without end effects, as e.g. in Fröhlich et $al.$ (1998), due to the irregular break up of the von Karman vortices. For the present configuration, however, it is substantially stronger and resembles the flow around a wall–mounted cube. Shah and Ferziger (1997), e.g., at $Re = 40000$ observed a fluctuating lift coefficient with $St \approx 0.1$ and pronounced irregularity in an LES of the latter.

4.5   Average flow

The average flow is now discussed, focusing on the results of run G2WS which previously were found to be in best agreement with the experiment. Figures 4 and 5 show streamlines from the LES and compare them to the corresponding experiment. Recall that LDA measurements cannot be performed close to solid walls due to shadowing and reflection of the laser beams so that no experimental data are available very near the cylinder. Behind the cylinder, the streamlines in the center plane exhibit a large recirculation region (see Figure 5) with the center of the vortex located at $x \approx 0.8, y \approx 2$ in the experiment and somewhat higher and closer to the cylinder in the LES. The length of the recirculation region in the simulation is similar to that in the experiment. Figures 4 and 5 also show calculated contours of velocity fluctuations in comparison with the experimental contours ($u-$fluctuations in a horizontal plane at $y/D = 1.5$ in Figure 4 and $v-$fluctuations in the vertical symmetry plane in Figure 5). Again the agreement is fairly good.

Figure 10 provides further information on the normal stresses $\langle u'u' \rangle$, $\langle v'v' \rangle$ and $\langle w'w' \rangle$ as well as the shear stress $\langle u'w' \rangle$ in wall-parallel planes. In order to address their change in the direction along the cylinder axis these quantities are given for $y/D = 1$ and $y/D = 2$, the latter being located half a diameter below the upper free end of the cylinder. In the lower plane it is obvious that $u-$fluctuations dominate in the separated shear layers while $v-$ and $w-$ fluctuations are maximal at or near the symmetry plane around $x/D = 2$. Comparison of these plots with the corresponding ones at $y/D = 2$ shows the substantial quantitative change the flow undergoes over this relatively short distance. Near the top, the recirculation is much shorter and all fluctuations are smaller because no pronounced shedding takes place here, as discussed before. Also, the $w-$fluctuations now exhibit their maximum in the centerplane. At $y/D = 1$, a tendency of the fluctuations for spreading away from the centerplane is observed for $x/D > 2$ which is due to the presence of the lower wall. The results of Figure 10 can also be compared to the data for a long cylinder obtained by Cantwell and Coles (1983) and reported in AGARD (1998). The Reynolds number $Re = 140000$ is by a factor of 3.3 larger which yields a shorter recirculation length, but the flow is qualitatively insensitive to the Reynolds number in this regime (Zdravkovich, 1997). Compared to these data, the present results feature a

wider distance of the separated shear layers. The maximum of $\langle u'u' \rangle$ appears at $z/D = 0.68$ instead of $z/D = 0.47$. The same holds for the maximum of the shear stress $\langle u'w' \rangle$ which is also located at a larger distance from the symmetry plane. Qualitatively different from the case of a long cylinder is the fact that the maximum of the normal stress $\langle w'w' \rangle$ is not attained in the center plane but at $z/D = 0.36$. Its value is 0.17 and hence substantially smaller than for a long cylinder (0.45 in Cantwell and Coles (1983)).

Figures 11 and 12 show streamlines in wall–adjacent cells along the cylinder surface and the bottom wall, respectively. The stagnation line running from $y/D = 0.2$ to $y/D = 2.1$ is clearly visible in the left oblique view of Figure 11. Near the bottom a saddle point exists at $y/D = 0.2$ resulting from the oncoming boundary layer. Along the stagnation line there is a slight upward motion, but on the side the lines remain fairly horizontal. Near the upper end the stagnation line splits up into a fan of streamlines due to the end effect. The separation line along the side wall is also visible. It is located at a fairly constant angle of 80 degrees from the stagnation line along the shaft, but curves towards the rear for $(H - y)/D < 1D$. Upstream of the curved separation line a pressure minimum with $c_P = (\langle p \rangle - p_\infty)/0.5\rho u_\infty^2) = -1.2$ is located at $y/D = 2.25$ and an angle of 70 degrees from the stagnation line. This observation corresponds to measurements of Uematsu and Yamada (1994) and Kawamura $et~al.$ (1984). The recirculating flow in the rear of the separation line exhibits a substantial upward motion as was to be expected from the streamlines directly behind the cylinder in Figure 5. At $y/D \approx 2.3$ and $z/D \approx \pm 0.3$ a focus on the surface is visible in the right picture of Figure 11 resulting from the upward rear motion and the counteracting downward motion in the center plane. On the roof, the flow separates at the front edge and reattaches around the center as evidenced by the plots in Figure 11. Figure 12 indicates the presence of a small horseshoe vortex in the average flow forming in front of the cylinder. In the companion experiment of Kappler (2002) no oil flow pictures were taken, but the behaviour just described corresponds qualitatively to the pictures taken by Hölscher (1993), which can be found in Majumdar and Rodi (1989), albeit for a cylinder placed in a much thicker boundary layer ($\delta/H = 2.54$).

The foci on the rear of the cylinder close to the top in the right part of Figure 11 are the footprints of two tip vortices which separate from the cylinder's free end and reach down into the wake (see Figure 1). The vortical motion in the average flow was visualized by means of a stream ribbon displayed in Figure 13. Its motion is somewhat irregular near the cylinder as it is caught in the horizontal vortex at $x \approx 0.8$, $y \approx 2$ discussed in relation to Figure 5 above. At a height of about $y/D \approx 1$ the stream ribbon leaves this vortex and stretches downstream until the exit of the domain, still spiralling but at a much lower pace. Two further streamtraces have also been introduced in close vicinity for clarification. The black one spirals in the interior of the ribbon's trace and indeed resembles the tip vortex in the sketches of Figure 1. The second, white one, remains further outward close to the ribbon but continues down to the bottom plate. So, on one hand the existence of the tip vortices on either side of the cylinder top sketched in Figure 1 is supported by the present results. In addition to this sketch we observe that the tip vortices do not persist further downstream but only reach downstream to about one diameter behind the cylinder. They are in fact part of an arch vortex with the shape of a reversed ∪ standing behind the cylinder. This vortex can be seen in the cuts along the center plane of Figure 5 due to the focus it generates closely behind the upper end where its axis is horizontal. The horizontal cuts at $y/D = 2$ and $y/D = 1$ in Figure 10 also show its axis which at these positions has become oblique at the upper and vertical at the lower position, respectively. The footprint of the arch vortex on the bottom plate is visible through the streamlines in Figure 12 exhibiting a focus at about the same $(x - z)$–coordinates

as in Figure 10(top,left). The arch vortex is a feature of the average, not the instantaneous flow and has similarly been observed in the flow around a surface–mounted cube (Martinuzzi and Tropea, 1993) simulated with LES in (Shah and Ferziger, 1997; Rodi *et al.*, 1997). Due to the circular geometry of the present body, the arch vortex exhibits a slightly different shape in its upper part compared to the flow around a cube and in this region in fact encompasses the tip vortices as visualized by Figure 13. This vortex should be included in sketches like the ones reproduced in Figure 1.

Figure 13 also allows to understand better the cuts at constant x/D displayed in Figure 6. The fact that the streamlines in these pictures do not always form closed lines, as would be the case in a two-dimensional flow for reasons of continuity, is due to the third velocity component in $x-$direction. At $x/D = 1$, the two foci result from the tip vortices visualized by the rapid spiralling part of the black lines in Figure 13. Their centers are located at about $y/D = 1.5$. The cuts at $x/D = 2$ in Figure 6, on the other hand, are located downstream of the arch–type vortex, roughly where the black streamtraces in leave the arch vortex horizontally in Figure 13, and here the tip vortices seem to disappear. Slightly further downstream, and for the case with slip already at $x/D = 2$, other vortex structures appear. The centers of these vortices are visible at $x/D = 3.5$ at an elevation of $y/D = 0.5 \ldots 0.8$. These trailing vortices are not continuations of the tip vortices and should also not to be confused with the horseshoe vortex since the latter is much smaller in the present case; furthermore, they also appear in the case with slip condition at the lower boundary which excludes the presence of a horseshoe vortex. Rather, these trailing vortices result from the strong downward motion behind the obstacle and the associated upward motion away from the centerplane caused by the finite width of the obstacle. This motion is illustrated in Figure 6 by streamlines (note that the arrows indicate only the flow direction and not the velocity strength) and the contour plot showing the magnitude of the secondary flow, i.e. the quantity $\sqrt{\langle v \rangle^2 + \langle w \rangle^2}$. The secondary velocity is maximal at $x/D = 2$ and decreases substantially further downstream. The maximum at $x/D = 3.5$ in the case with wall is 0.3. Hence, the resulting spiraling motion is relatively weak compared with the average $u-$velocity which for example is $\langle u \rangle = 0.7$ in the centers of both vortices in this picture. This is also reflected by the slow turning of the stream ribbon in Figure 13.

5 Conclusions

We have presented several LES of the flow around a surface–mounted cylinder of finite height. A detailed comparison to a companion experiment has shown that the results obtained with the Smagorinsky subgrid–scale model capture the main features of this complex flow quite well. The results reveal the details of the complicated vortex dynamics where separation from the sidewalls and the roof of the cylinder interact closely. The relatively small height of the cylinder does not allow the development of straight, two–dimensional von Karman vortices, but these are bent and distorted as they travel along the wake. The average flow is shown to exhibit an arch–type vortex behind the cylinder as observed in the flow around a wall–mounted cube. This has not been reported previously in the literature on the subject. Further investigations might be concerned with its dependence on the height–to–diameter ratio.

References

AGARD (1998). A selection of test cases for the validation of Large Eddy Simulations of turbulent flows, AGARD–AR–345.

Baban, F. and So, R. (1991). Aspect ratio effect on flow-induced forces on circular cylinders in a cross flow. *Exp. in Fluids*, **10**, 313–321.

Breuer, M. and Rodi, W. (1996). Large eddy simulation of complex turbulent flows of practical interest. In E. Hirschel, editor, *Flow simulation with high performance computers II*, volume 52 of *Notes on Numerical Fluid Mechanics*, pages 258–274. Vieweg, Braunschweig.

Cantwell, B. and Coles, D. (1983). An experimental study of entrainment and transport in the turbulent near wake of a circular cylinder. *J. Fluid Mech.*, **136**, 321–374.

Farivar, D. (1981). Turbulent uniform flow around cylinders of finite length. *AIAA journal*, **19**, 275–281.

Fröhlich, J., Rodi, W., Kessler, P., Parpais, S., Bertoglio, J., and Laurence, D. (1998). Large eddy simulation of flow around circular cylinders on structured and unstructured grids. In E. Hirschel, editor, *Numerical Flow Simulation I*, volume 66 of *Notes on Numerical Fluid Mechanics*, pages 319–338. Vieweg.

Fröhlich, J., Rodi, W., Bertoglio, J., Bieder, U., and Touil, M. (2001). Large eddy simulation of flow around circular cylinders on structured and unstructured grids, II. In E. Hirschel, editor, *Numerical Flow Simulation II*, volume 75 of *Notes on Numerical Fluid Mechanics*, pages 231–249. Vieweg.

Fröhlich, J., Rodi, W., Dewan, A., and Fontes, J. (2002). Large eddy simulation of flow around the free end of a circular cylinder. In E. Hirschel, editor, *Numerical Flow Simulation III*, volume 82 of *Notes on Numerical Fluid Mechanics*, pages 191–202. Springer.

Germano, M., Piomelli, U., Moin, P., and Cabot, W. (1991). A dynamic subgrid–scale eddy viscosity model. *Phys. Fluids A*, **3**, 1760–1765.

Hölscher, N. (1993). *Ein multivariater Ansatz für die aerodynamische Übertragungsfunktion der Winddrücke in atmosphärischer Grenzschichtströmung*. Ph.D. thesis, Ruhr–Universität Bochum.

Jordan, S. (2002). Investigation of the cylinder separated sher–layer physics by large–eddy simulation. *Int. J. Heat Fluid Flow*, **23**, 1–12.

Kappler, M. (2002). *Experimentelle Untersuchung der Umströmung von Kreiszylinder mit ausgeprägt dreidimensionalen Effekten*. Ph.D. thesis, Institute for Hydromechanics, University of Karlsruhe.

Kawamura, T., Hiwada, M., Hibino, T., Mabuchi, I., and Kamuda, M. (1984). Flow around a finite circular cylinder on a flat plate. *Bulletin of the JSME*, **27**(232), 2142–2151.

Majumdar, S. and Rodi, W. (1989). Three-dimensional computation of flow past cylindrical structures and model cooling towers. *Building and Environment*, **24**(1), 3–22.

Martinuzzi, R. and Tropea, C. (1993). The flow around a surface–mounted prismatic obstacle placed in a fully developed channel flow. *J. Fluid Eng.*, **115**, 85–92.

Meyers, J., Geurts, B., and Baelmans, M. (2003). Database analysis of errors in lerge–eddy simulation. *Phys Fluids*, **15**, 2740–2755.

Moin, P. and Kim, J. (1982). Numerical investigation of turbulent channel flow. *J. Fluid Mech.*, **118**, 341–377.

Naudascher, E. and Rockwell, D. (1994). *Flow-induced vibrations: An engineering guide.* IAHR Hydraulic Structures Design Manuals. Balkema Publishers, Rotterdam.

Okamoto, S. and Sunabashiri, Y. (1992). Vortex shedding from a circular cylinder of finite length placed on a ground plane. *J. Fluids Eng*, **114**, 512–521.

Okamoto, T. and Yagita, M. (1973). The experimental investigation on the flow past a circular cylinder of finite length placed mormal to the plane surface in a uniform stream. *Bulletin of the JSME*, **16**(95), 805–814.

Rodi, W., Ferziger, J., Breuer, M., and Pourquié, M. (1997). Status of large eddy simulation: Results of a workshop. *J. Fluid Eng.*, **119**, 248–262.

Shah, K. and Ferziger, J. (1997). A fluid mechanicians view of wind engineering: Large eddy simulation of flow past a cubic obstacle. *J. Wind Eng.*, **67 & 68**, 211–224.

Uematsu, Y. and Yamada, M. (1994). Aerodynamic forces on circular cylinders of finite height. *J. Wind Eng. and Ind. Aerodyn.*, **51**, 249–265.

Werner, H. and Wengle, H. (1993). Large–Eddy Simulation of turbulent flow over and around a cube in a plane channel. In F. Durst, R. Friedrich, B. Launder, F. Schmidt, U. Schumann, and J. Whitelaw, editors, *Selected Papers from the 8th Symposium on Turbulent Shear Flows*, pages 155–168. Springer.

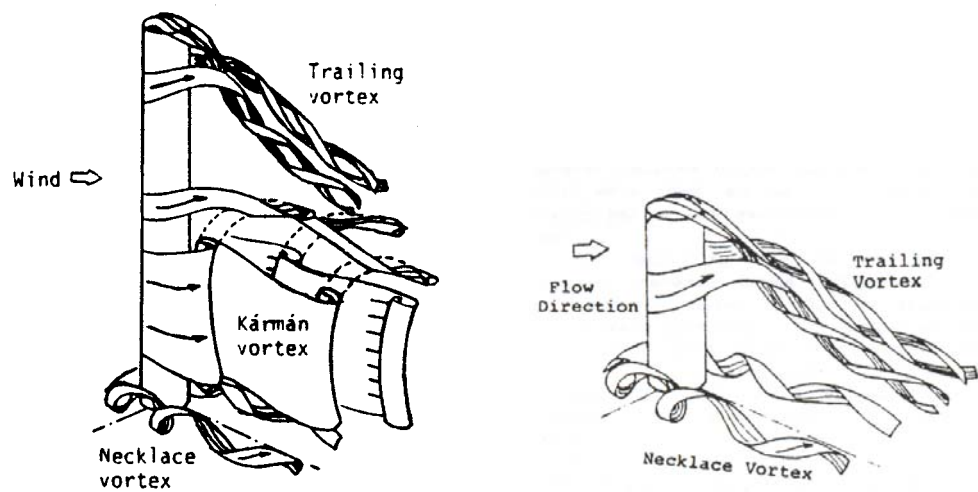Zdravkovich, M. (1997). *Flow Around Circular Cylinders*. Oxford University Press.

Figure 1: Sketches of the flow field around a cylinder of finite height from Kawamura *et al.* (1984). Left: situation if the cylinder is longer than the critical length for vortex shedding, right: the same if the cylinder is shorter.
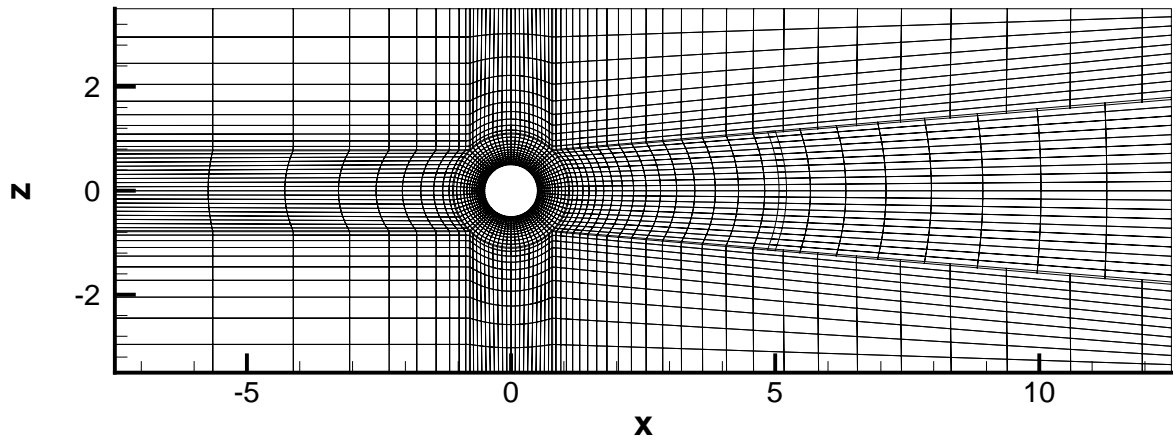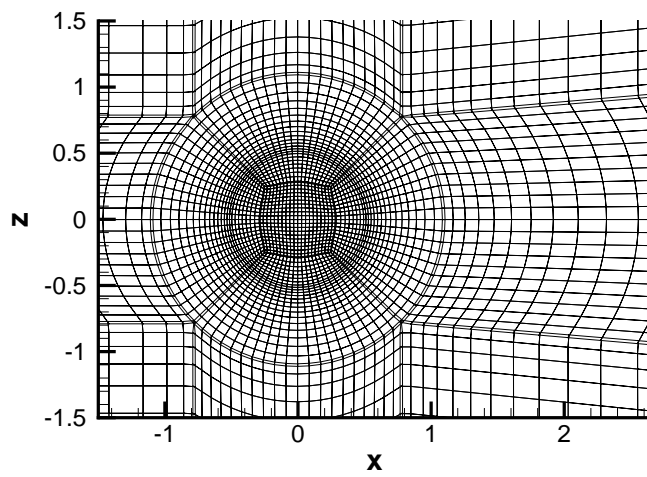
11

Figure 2: Two–dimensional cuts in wall–parallel direction through grid G2. The bottom picture shows the entire domain while the top picture displays a zoom of the grid above the cylinder. Only every 4th point is plotted (the complete grid has no hanging nodes).
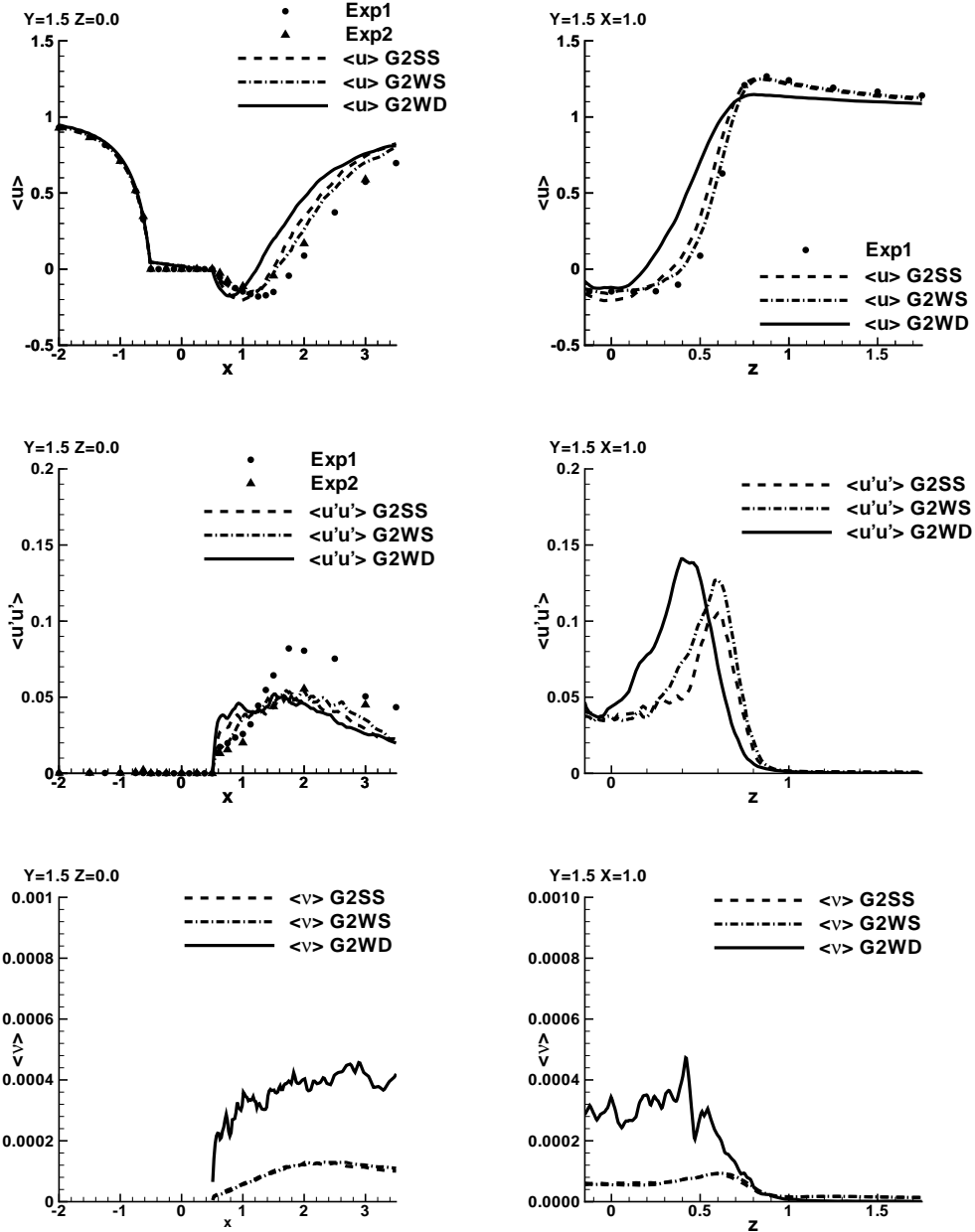
Figure 3: Average quantities along lines at an elevation $y/D = 1.5$ above the bottom wall. Left: in the center plane with $z/D = 0$. Right: in lateral direction at $x/D = 1$. Streamwise mean velocity (top) and corresponding fluctuations (middle) and average turbulent viscosity (bottom). Lines: LES, symbols: experimental data from Kappler (2002).

13
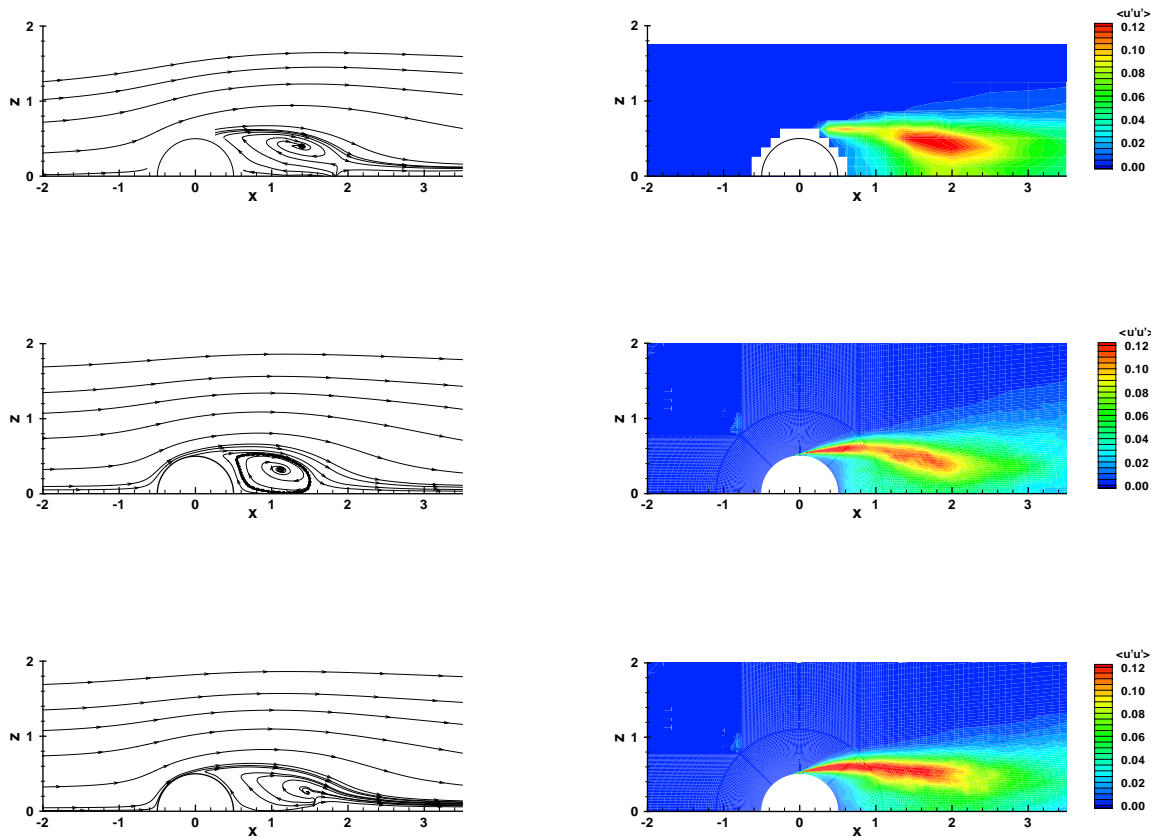
Figure 4: Average streamlines at $y/D = 1.5$ (left) and $\langle u'u' \rangle$ in the same plane (right). The scale in the contour plots ranges from 0 to 0.12. Top: experiment, middle: run G2SS, bottom: run G2WS.

14
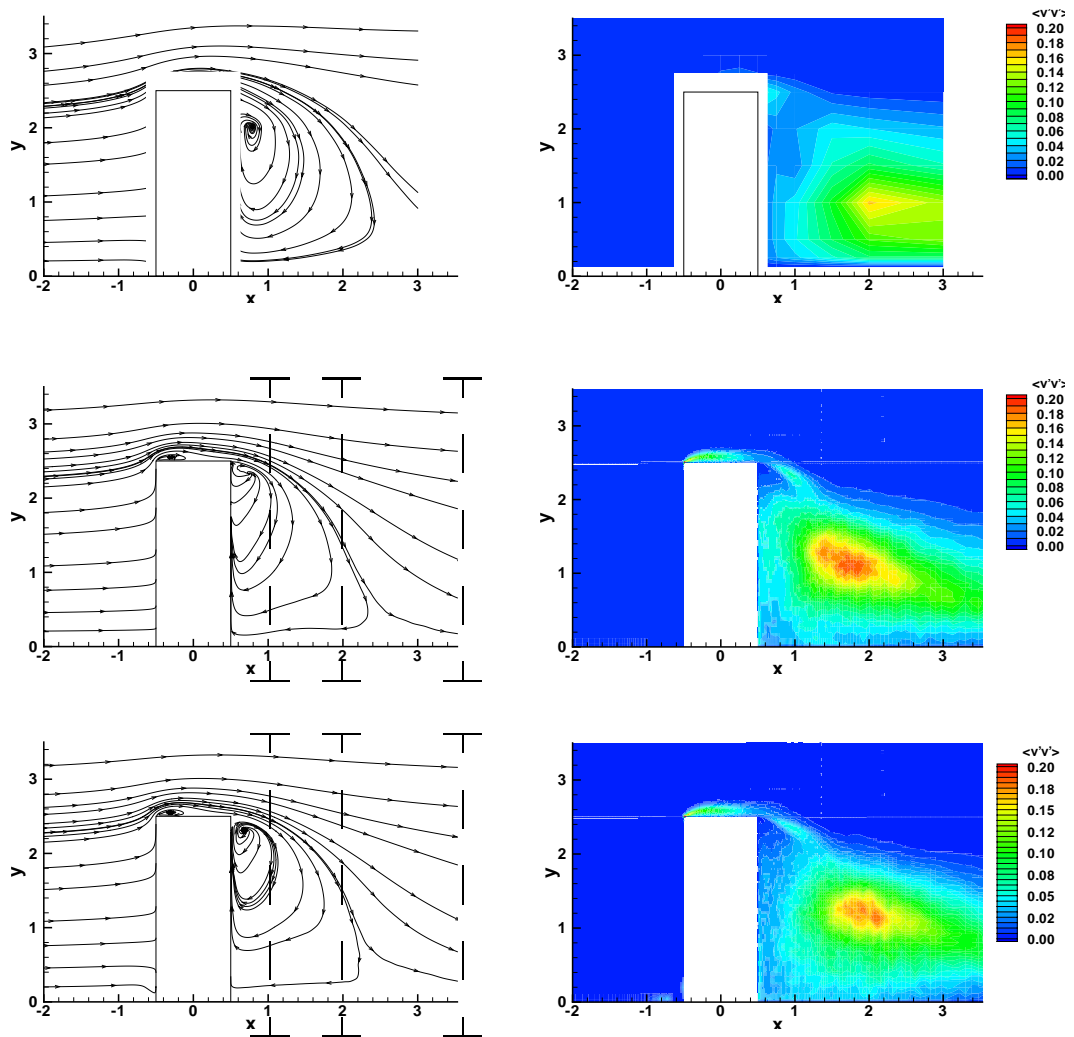
Figure 5: Average streamlines (left) and vertical fluctuations $\langle v'v' \rangle$ (right) in the centerplane $z/D = 0$. The colour scale ranges from 0 to 0.2. Top: experiment, middle: run G2SS, bottom: run G2WS. The dashed lines in the streamline pictures indicate the locations for which $z-y-$cuts are displayed in Fig. 6.
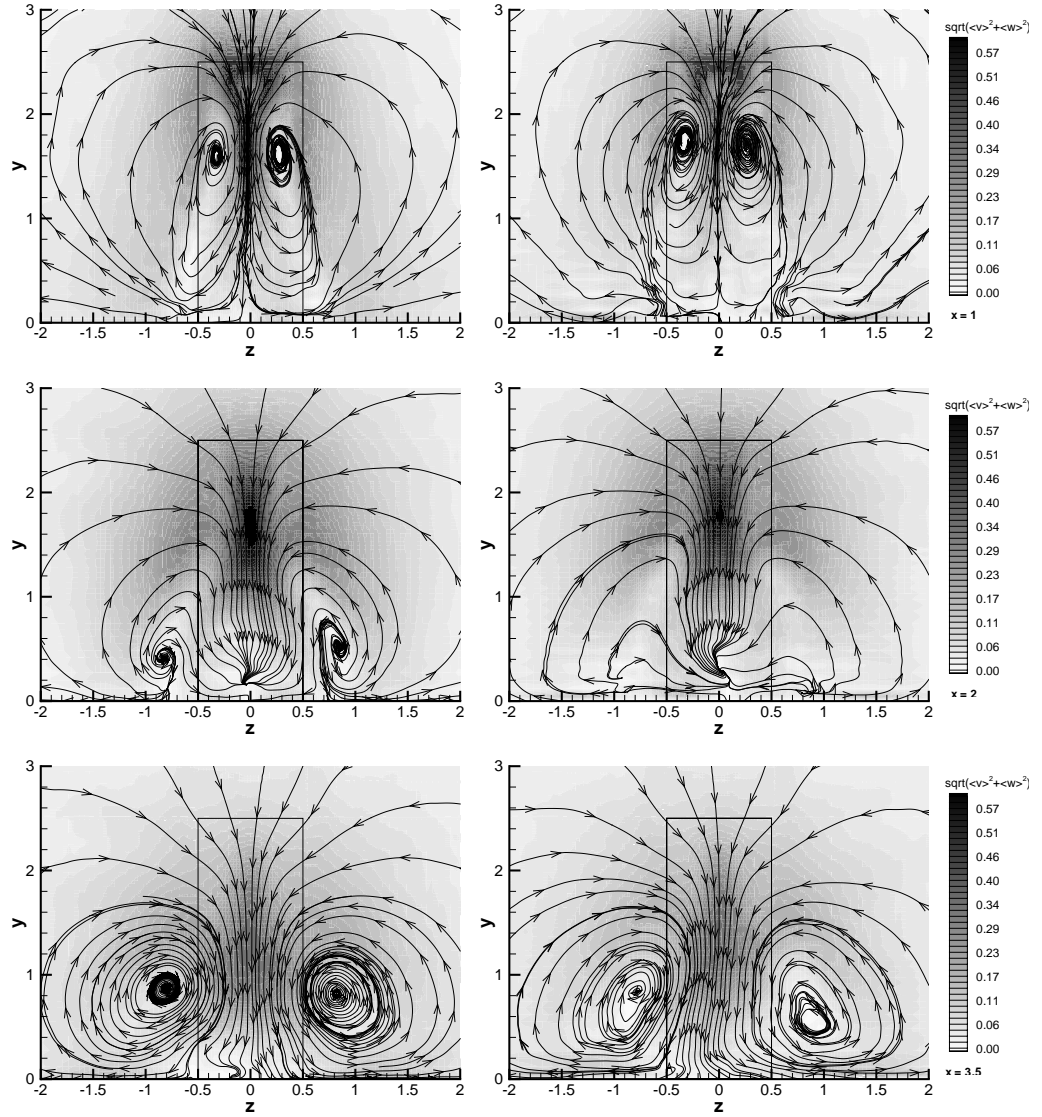
Figure 6: Average flow structure in planes normal to the $x-$axis behind the cylinder at $x/D = 1$ (top), $x/D = 2$ (middle), $x/D = 3.5$ (bottom). Average streamlines are shown together with the magnitude of the secondary flow, $\sqrt{\langle v \rangle^2 + \langle w \rangle^2}$, represented by the gray scale. Left: computation with slip condition (run G2SS). Right: the same data with a solid wall (run G2WS). The location of these cuts is indicated in Figure 5.
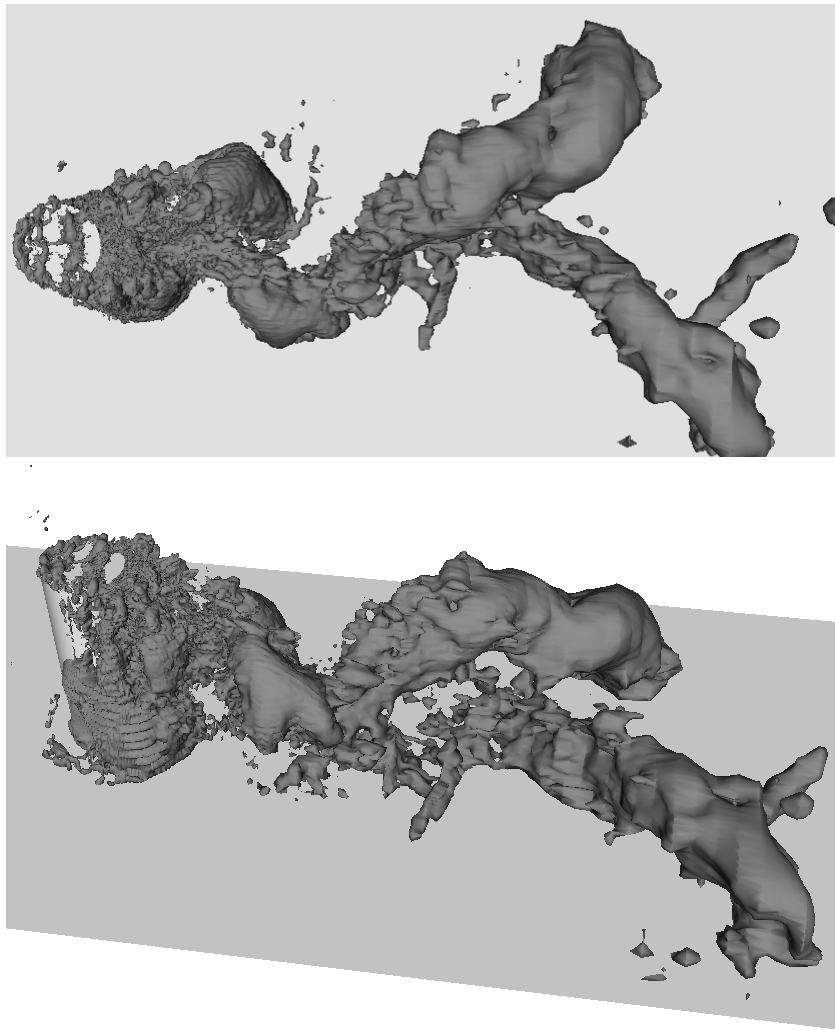
Figure 7: Instantaneous flow structures obtained from G2WS Iso–surface of the instantaneous pressure deviation, $\tilde{p}' = -0.05$, viewed from the top and at an oblique angle from the rear.
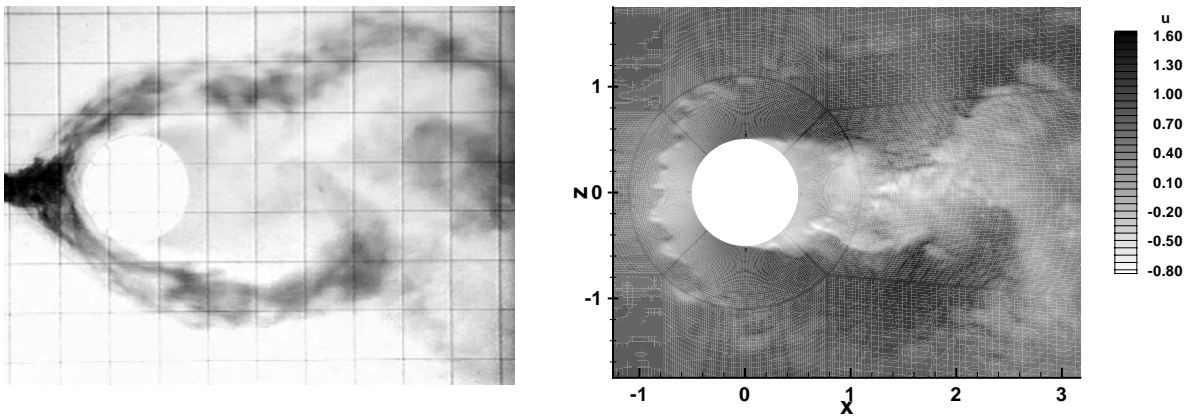
Figure 8: Instantaneous picture of vortex shedding close to the ground plate. Left: visualization by means of a tracer in the experiment Kappler (2002), right: instantaneous $u-$velocity in the wall–adjacent cell from run G2WS.
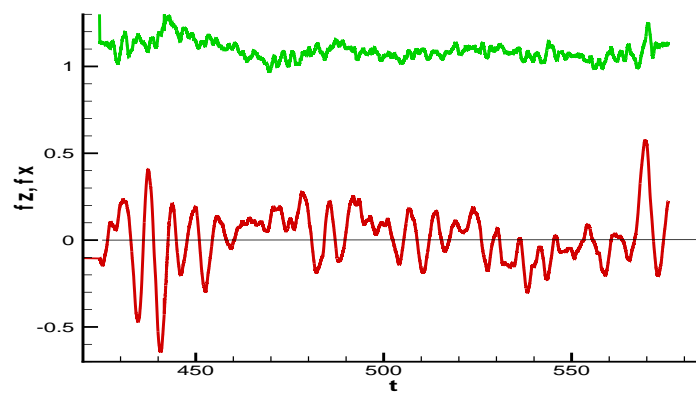
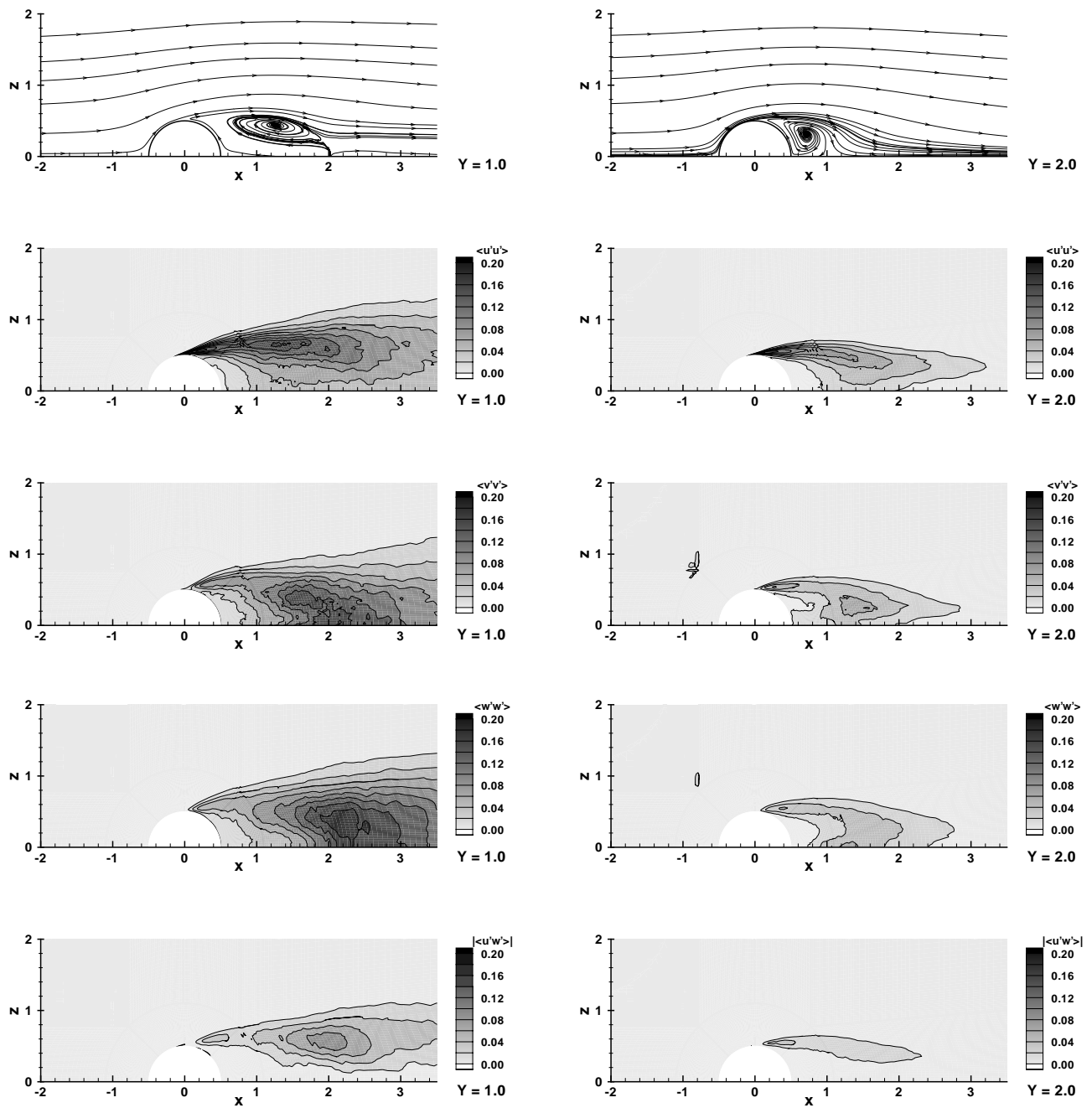Figure 9: Lift force f_z (lower curve) and drag force f_x (upper curve) for run G2WS.

Figure 10: Streamlines and resolved stresses $\langle u'u' \rangle$, $\langle v'v' \rangle$, $\langle w'w' \rangle$ and $|\langle u'w' \rangle|$ from run G2WS (top to bottom). The solution is depicted in planes at $y/D = 1$ (left) and $y/D = 2$ (right). The gray scale ranges from 0.0 to 0.2 with increments of 0.02.
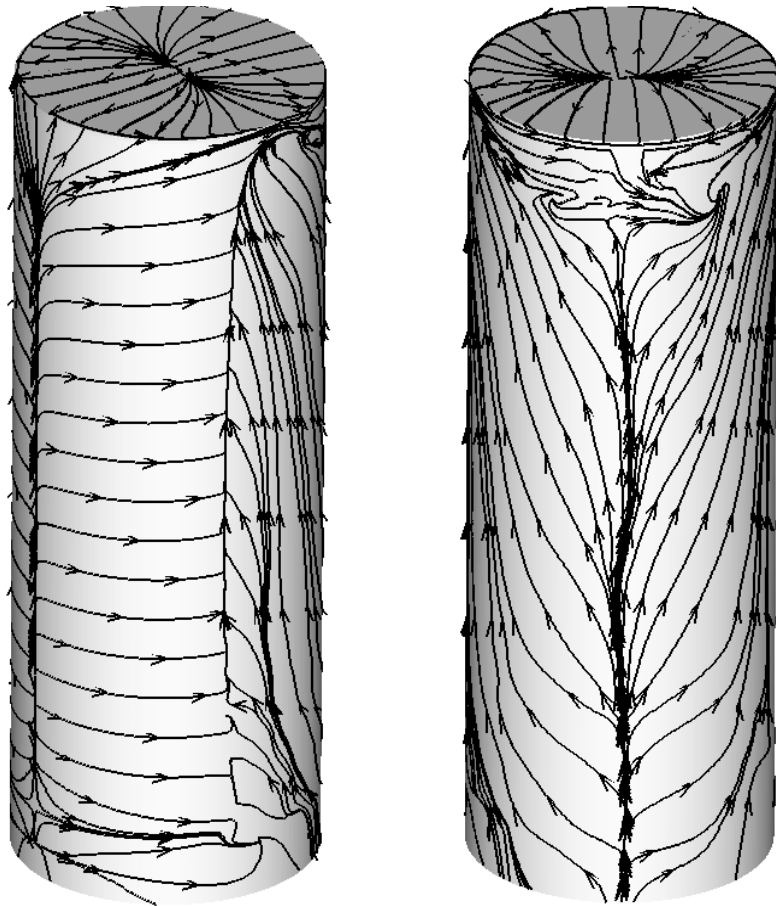
20

Figure 11: Surface streamlines from run G2WS. Left: oblique view with flow from left to right. Right: rear view.
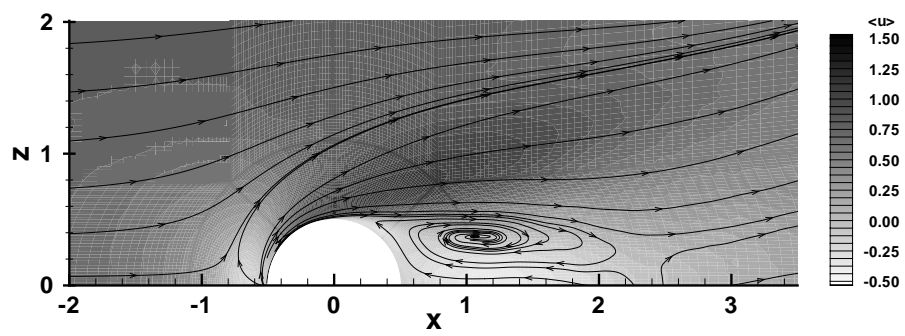
Figure 12: Average streamlines in the wall–adjacent cell along the bottom wall from run G2WS. The color scale represents the average streamwise velocity component.
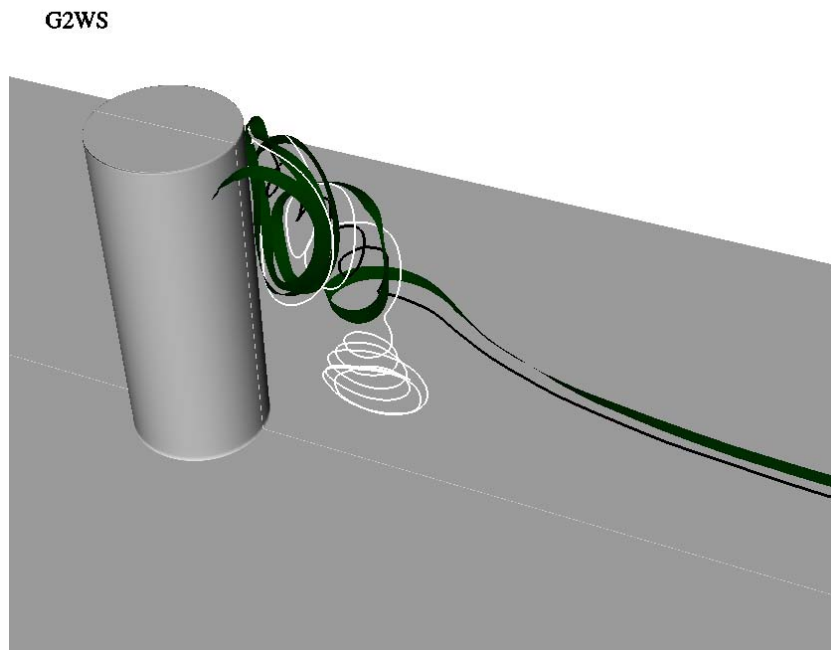
Figure 13: Visualization of the vortex structure in the average flow behind the cylinder (run G2WS).

Table 1: Overwiew over the simulations performed: number of grid points, bottom–wall boundary condition, the subgrid–scale modelling (SM=Smagorinsky model, DSM=dynamic model), averaging time t_a, and mean drag coefficient C_D.

Run	grid	bottom	SGS	t_a	C_D
G1SS	$1.0\,10^6$	slip	SM	155	0.32
G2SS	$6.4\,10^6$	slip	SM	123	0.88
G2WS	$6.4\,10^6$	WW	SM	100	0.88
G2WD	$6.4\,10^6$	WW	DSM	83	0.6